Brain-wide monosynaptic connectivity mapping with ROInet-seq

Zhige Lin[1], Osnat Ophir[1], Thorsten Trimbuch[2, 3], Bettina Brokowski[2, 3], Muhammad Tibi[1], Polina Pavletsov[1], Hermann Schmidt[5], Christian Rosenmund[2, 3, 4], Hannah Hochgerner[1, 6], Amit Zeisel[1, 6]

[1] Technion – Israel Institute of Technology, Faculty of Biotechnology and Food Engineering, 320003 Haifa, Israel
[2] Viral Core Facility, Charité-Universitätsmedizin, Berlin 10117, Germany.
[3] Institute of Neurophysiology, Charité-Universitätsmedizin, Berlin 10117, Germany.
[4] NeuroCure Cluster of Excellence, Charité-Universitätsmedizin, Berlin 10117, Germany
[5] DNA Cloning Service, Hamburg, Germany

[6] Correspondence to amit.zeisel@technion.ac.il (lead contact), hhoch@campus.technion.ac.il | ***zeisellab.org***

Viral projection tracing strategies help establish regional connectomes of mammalian brains. Monosynaptic connectivity tracing with G-deleted rabies virus (RV) establishes retrograde synaptic connectivity, but cannot distinguish networks at cell resolution. We developed ROInet-seq, an accessible spatial method using barcoded ΔG rabies virus, amenable to readout by RNA-sequencing. We optimized library complexity and uniformity, such that detection of specific barcodes can reliably distinguish multiple infected neurons, and their individual monosynaptic input networks. In cortical brain areas we found preserved regional network motives, including co-inputs to single cortical neurons from distant and local sites. Towards improved spatial resolution and simultaneous detection of the single cells' transcriptomes and networks, we finally sampled barcoded ΔG rabies virus infected hippocampus on a commercial spatial transcriptomics assay and reveal details of the regions' neurons local network architecture.

Introduction

Neuronal networks are the biological basis for all higher functions and behaviours in animals. Tasks such as memory acquisition and retrieval, or sensing and processing social cues, require extraordinary flexibility, versatility and computational power. These capabilities are achieved by the brain's multiregional circuits and local modifying networks of neurons, but revealing the architecture of their networks remains a major undertaking. To map neuronal networks brain-wide, large efforts have been applied across different scales of connectivity. For example, great efforts are undertaken to visually reconstruct detailed maps of single neurons and their complete synaptic connectivity using transmission electron microscopy (EM (Mahalingam et al. 2022; Turner et al. 2022; Yin et al. 2020)), or expansion microscopy (e.g., ExM/STEDm (Michalska et al. 2023)). Naturally, these approaches remain highly complex and costly. Further, electrophysiology approaches such as Patch-Seq (Fuzik et al. 2016) can measure neural connectivity and identity simultaneously. However, this method is typically limited to several pairs of neurons, and the inability to measure long-range projections, such as connections between distant brain regions, makes it challenging to obtain a complete map of single-cell neuronal connections. On the other end of the scale, viral projection tracing uses modified neurotrophic virus, such as fluorescent marker-expressing adeno-associated virus (AAV). Depending on the virus' tropism, the region of interest's input or output regions are then fluorescently labelled, revealing brain-region connectivity on a mesoscale level (Oh et al. 2014; Qiu et al. 2024). However, these maps generally do not reveal synaptic connectivity, and lack single-neuron resolution.

In sum, neither viral projection tracing, Patch-Seq, nor EM, can feasibly describe synaptic neuronal networks on a single-neuron scale, across substantial volumes of a mammalian brain. Transsynaptic viral tracing strategies circumvent some limitations of these approaches, by visually labelling neurons that are synaptically connected to each other. To map synaptic input networks, a genetically modified virus (for example, G-deleted rabies virus (ΔG-RV) (Wickersham et al. 2007)), is injected to a site of interest (start site), and when provided with G *in trans*, can transfer to input neurons via its synapses. In this manner, ΔG-RV labels neurons infected in the start site -and their input neurons, revealing monosynaptic-connected input networks. The approach enables mapping the brain's wiring architecture in great volume *in vivo*, and when multiple fluorophores and selective receptors are used, independent circuits can be revealed in mutliplex (Suzuki et al. 2020). But in the traditional usage of ΔG-RV, multiple cells are labeled with the same fluorescence tag, which hinders distinguishing input networks of single neurons in the brain. Similar to a modification used in non-synaptic multiplex virus tracing (X. Chen et al. 2019; Kebschull et al. 2016), several groups recently developed a variant of ΔG-RV that carries genetic barcodes to increase the number of distinguishable markers that uniquely label individual networks in a single experiment. This allowed to track glial interactions (Clark et al. 2021) and monosynaptic retrograde neuronal connectivity *in vitro* (Saunders et al. 2022) and *in vivo* (Zhang et al. 2023). For example, (Zhang et al. 2023) used *in situ*-sequencing to read network barcode sequences, and characterize the cells' molecular identities, besides providing valuable spatial context of single cells in the network. This method is practically limited to small areas or local networks, and highly costly to implement at scale. Despite these limitations, the genetic barcoding strategy shows great potential in improving the resolution and scale of neuronal connectivity mapping.

Here, we generated high-complexity libraries of distinguishable rabies virus particles by inserting a 21-nt random barcode into the 3'UTR region of RV-*M* gene. We showed that droplet-based scRNA-seq could detect network barcodes and cell transcriptomes of *in vivo* networks simultaneously. We then developed an accessible, coarse spatial assay, compatible with standard histology- and molecular biology tools; that allowed reconstruction of virtually single-neuron input networks at low sequencing costs. Finally, we demonstrated how a commercial spatial transcriptomics assay of higher resolution (Visium ST) can improve the method's detection of local networks in densely wired brain regions. Our study reveals quantitative and qualitative insights into cortical and hippocampal connectivity; including the robust occurrence of simultaneous inputs from multiple distal sites to a single cortical cell, and distinct, region-specific network cytoarchitectures.

Results

To insert a 21-nt random barcode to the RV genome at an optimal position, we first tested the genome's coverage in ΔG-RV-infected HEK cells using droplet-based 3'scRNA-seq by 10xGenomics. Of five genes in the ΔG-rabies genome (*N, P, M, GFP* and *L*), matrix protein-encoding *M* achieved the highest coverage, and we inserted the barcode at its 3'UTR (Fig. 1A). Then, rabies particles were recovered from HEK-cell transfection with the barcoded ΔG-RV plasmid library, and pseudotyped with the avian envelope EnvA (Fig. 1B), as described before (Osakada and Callaway 2013). For uniform

representation of all barcodes in the libraries of RV plasmids and particles it was vital to eliminate bias introduced at any step of the protocol (Fig. 1C-D). Low-complexity and/or non-uniform libraries, such as when few barcodes are overrepresented, would lower the confidence that a given detected barcode in fact represents a single, initially infected starter cell. Therefore, we first introduced several measures to achieve highly upscaled, uniform RV plasmid and particle production (see Methods).

For example, to maximize RV particles titer for in vivo tracing, plasmid-transfected HEK cells are typically amplified multiple times. However, during amplification, any fast-growing subset of cells would lead to an overrepresentation of the barcodes it produces. Highly amplified particles then occupy a large portion of the entire library (high frequency), and depending on sequencing depth, would in practice reduce overall library complexity (e.g., library 16.1, Fig. 1C-D). To overcome this limitation in subsequent RV-ΔG-BC libraries, HEK cells were transfected with the RV-plasmid library on a large, parallel scale and we limited production time to a single round, rather than amplifying cells multiple times (e.g., libraries 16.4, 16.5, 16.6, 17.2; Fig. 1C-D). This balanced cell growth, and drastically improved uniformity of the barcoded viral particles library. The optimized production strategy resulted in final libraries with acceptable uniformity: Measured by UMI-based amplicon sequencing, the top barcodes occupied ~0.1-1% of the total library, and the probability of multiple cells infected by the same barcode at infection of around 200 starter cells was 10% or less (Fig. 1C-D).

We observed 2-6× lower titers of BC-ΔG-RV in virus production, hinting that insertion of a 21nt barcode to the 3'site of *M* may have compromised the virus' replication or packaging capacity. Therefore, we next tested whether *in vivo* retrograde transfer efficacy may have been compromised, too. Indeed, compared to standard ΔG-RV, the barcoded ΔG-RV showed overall lower labeling efficacy of neurons in the mouse hippocampus CA1, and decreased efficiency of monosynaptic transmission to CA1 input cells (i.e., presynaptic-per-starter cells). At the same time, variability between animals and experimental batches was large for both virus variants (Fig. S1).

To assess how BC-ΔG-RV performs at cell resolution *in vivo*, we isolated BC-ΔG-RV-infected cells for single-cell RNA-seq (Fig. S2). We harvested one brain 8 days after BC-ΔG-RV injection to the CA1, then gently microdissected and dissociated fluorescent regions. Cell suspensions were quickly fixed, FACS sorted, and BC-ΔG-RV (GFP+) cells processed for scRNA-seq (10x Chromium). Out of 6310 recovered neurons, 66.4% cells contained BC-ΔG-RV, and 1.4% were confirmed starter cells (i.e., they also expressed genes derived from the AAV helper virus). This means that on average each starter cell transynaptically labelled 47.4 input cells ("presynaptic-per-starter"), which was in line with quantifications from imaging (Fig. S1). Starter cells were predominantly glutamatergic cortical-, or hippocampal pyramidal cells, although the lower transcriptome quality of RV-infected cells compromised finer subtyping (Fig. S2). We observed that in the start site, infection with multiple particles (multiple BCs) was nearly as common as single BC-infected starter cells (45% of all start cells had >1 BC, Fig. 1F, Fig. S2). And even that 34% of all RV+ cells had >1 BC (Fig. S2), most of these had BC combinations that did not overlap with those observed in any individual starter cell; but likely resulted from participating in multiple networks. Only in a minority of cases did we observe that multi-BC infected starter cells transferred more than one BC to their input networks (Fig. 1G). For

example, out of 30 starter cells with 2 BCs, 76% transferred only one BC to input neurons. The same combination of 2 BCs was only detected in 7 input networks; and per network, in no more than 3 neurons; well below the average network size. Observing the same cell's connection multiple times – due to multi-BC infection – thus likely accounts only for a minority of cases and is unlikely to overestimate connectivity.

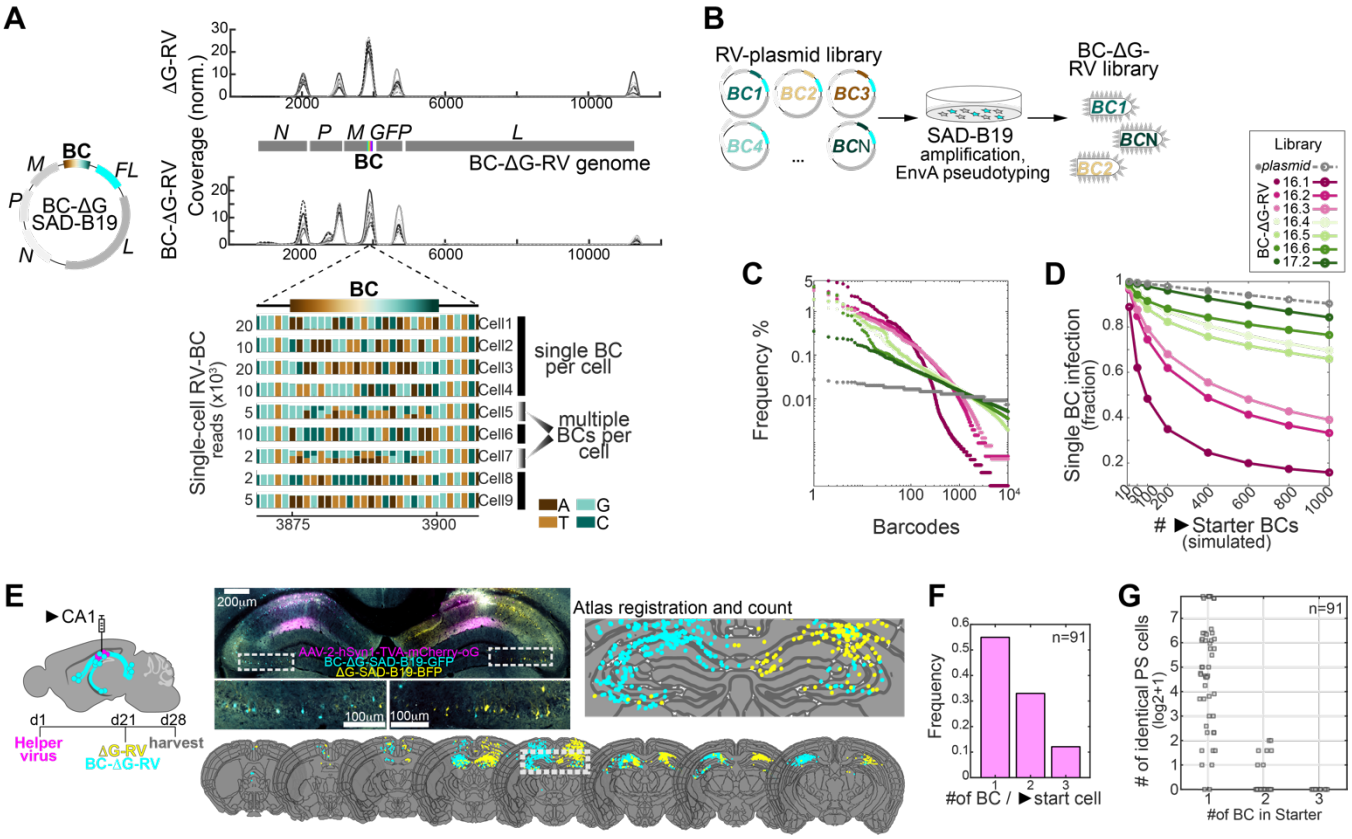

Figure 1 | Generation of barcoded delta-G rabies virus and *in vivo* application for network tracing. (**A**) A 21nt random barcode was inserted to the 3' site of the highly detected M-gene in G-deleted (ΔG) SAD B19 rabies virus. Right, coverage of the rabies genome in 10xChromium 3' scRNA-seq in ΔG-RV, and BC-ΔG-RV. Below, reads in the BC region from 9 single BC-DG-RV-infected cells, detected by 10xChromium 3' scRNA-seq. Most cells contained a single barcode, others contained multiple barcodes. (**B**) The BC-DG-RV library is recovered, amplified and pseudotyped with avian envelope (EnvA). (**C**) Frequency of the top 10^4 detected barcodes in the RV-plasmid library and increasingly more complex BC-ΔG RV libraries. (**D**) Simulation of the expected cell fraction with singlet infection of increasingly more complex BC-ΔG RV libraries, and hypothetic comparison to the RV-plasmid, as a function of starter cells number. (**E**) Comparison of ΔG-RV and BCΔG-RV *in vivo*. Equal titers (0.8×10^8IU/ml) of BC-ΔG-SAD-B19-GFP and ΔG-SAD-B19-BFP control, injected to unilateral CA1, each, display similar infection and transmission patterns. (**F**) Frequency of detecting single or multiple BCs in a single starter cell (91 neurons). (**G**) Scatterplot of 91 verified starter neurons, with 1, 2 or 3 unique BCs detected, and the indicated number of presynaptic cells with that same BC combination.

Next, we aimed to apply BC-ΔG-RV to characterize single-neuron input networks *in vivo.* Here, we assume that each barcode virtually represents a single neuron, based on the following observations: 1. Each start cell is dominantly infected by one or several barcoded

RV-particles, where only one is likely to be transferred to most input neurons. 2. The BC library is highly complex, such that BCs can serve as a unique molecular tag. 3. BCs can be captured and reliably read by a universal RNA-seq protocol. Therefore, with good characterization of BC-ΔG-RV *in vivo* performance and important improvements in library uniformity, we concluded that detection of a unique BC in a cell or region *in vivo* faithfully describes synaptic input of that cell or region to the start site. We argued that reconstructing input networks to a start site of interest required a sensitive, accessible method scalable to the full volume of the brain. Therefore, we developed "region of interest-network sequencing", or ROInet-seq, where we specifically sequenced all barcodes from individual BC-ΔG-RV-infected regions after full-volume fluorescent imaging. Briefly, 7d after BC-ΔG-RV surgeries, brains were harvested by transcardial PFA-perfusion, cryoprotected, cryosectioned (50μm), mounted and imaged (Fig. 2A-B). Based on the images, we selected ROIs, then microdissected and collected each ROI to lysis mix (Fig. 2C-D, Fig. S3). All transcripts were captured with an individually indexed poly-T capture oligo (ROI-barcode), reverse transcribed, then the RV-*M*-gene (flanked by the BC sequence) was specifically amplified. Finally, ROIs were pooled and processed for sequencing (Fig. S3 and Methods).

Each experiment resulted in an array of unique BCs detected in *N* ROIs, where each unique BC was detected in one, or multiple ROIs (Fig. 2E). From this, we extracted a matrix of pairwise BC overlaps over all regions (Fig. 2F), to visualize to what extent any two ROIs share unique BCs (i.e., connect to the same starter cells). For example, a ROI that gave input to the experiment's start site would share BCs with the start site (**A**). Further, since for each ROI we recorded both the count of fluorescent labelled cells and the number of detected BCs, we could use their ratio (FL+/BC) to represent average connectivity patterns (Fig. 2F). For any given ROI, we distinguish three scenarios with regards to this ratio: (i) *feedforward* ($N_{BC}=N_{FL+}$), where on average, each neuron is connected to one starter cell and they each carry one unique BC; (ii) *divergence* ($N_{BC}>N_{FL+}$), where on average each input cell is connected to more than one starter cell, and (iii) *convergence* ($N_{BC}<N_{FL+}$), where on average several FL+ cells input to the same starter cell. The ratio represents an average, qualitative measure; since (i) in any ROI, we detect the bulk of that ROI's BCs, and (ii) sequencing depth and imaging thresholds may vary between individual experiments. Yet, each of these distinct patterns may represent a different modality of connectivity and information flow.

In addition, ROInet-seq is uniquely able to capture higher order networks; i.e., subnetworks where several remote neurons are presynaptic to a given single neuron in start site. This can be observed as detection of a BC in more than one input ROI (**B**) describes co-input of neurons from multiple regions to the same single cell in the start site. Finally, not all BCs that transsynaptically labelled neuronal input networks may be detected in the start site at the time of sampling ("ghost" BCs). Ghost barcodes likely result from cytotoxicity in RV-infected cells, affecting start cells before input cells. However, BCs could only stem from start sites, and possible sequencing errors were conservatively corrected for. Therefore, assuming that each detected BC represents a single starter cell ("ghost" or active), allows ROInet-seq to visualize input subnetworks of each BC, or show the sum for a given injection site.

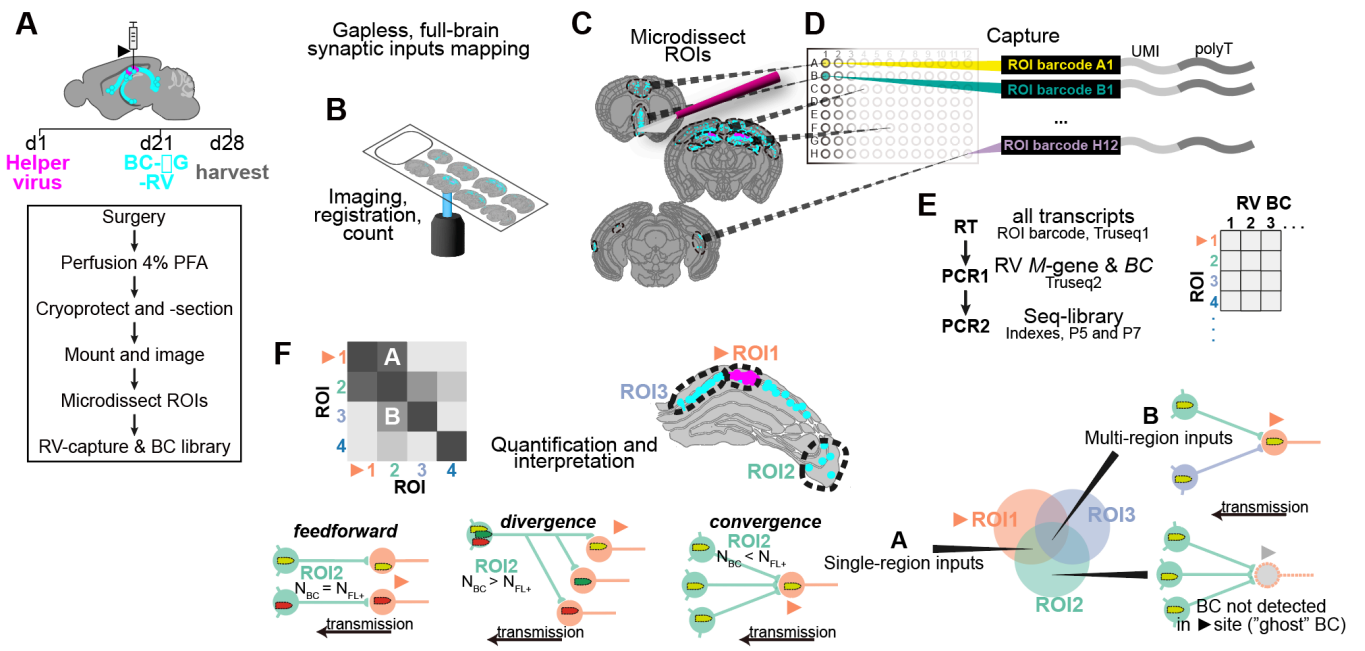

Figure 2 | ROInet-seq for full-volume cell-resolved region-of-interest input network maps to the CA1. (**A**) Experimental outline; on top; helper virus (day 1), and BC-DG-RV (day 21) to the CA1 start site, and harvest day 28 by 4%PFA perfusion. Brains are postfixed, cryoprotected, cryosectioned, mounted, imaged, and ROInets registered and quantified (**B**). ROIs are microdissected (**C**), and transferred to individual wells in a multiwell plate containing lysis buffer with barcoded polyT-capture oligos (**D**), to introduce a single barcode to all poly-adenylated of the same ROI. (**E**) Reverse transcription, targeted PCR to amplify the RV *M* gene with the BC fragment, and PCR for final sequencing libraries. Sequencing results in a list of unique detected ΔG-RV barcodes per ROI. (**F**) Barcode detection in multiple ROIs allows to reconstruct (higher-order) monosynaptic input networks, visualized using three hypothetical ROIs with overlapping BC-detection in the hippocampus. The ratio of cells detected RV-positive by fluorescence imaging vs. BCs detected in sequencing helps distinguish input network motifs. Not all BCs detected in input sites are also detected in start sites ("ghost" BCs).

We first targeted the somatosensory cortex (SSp Fig. 3A-B, Table S1), imaged, and collected 18 ROIs for BC-sequencing, including five that resulted from an off-target start site in the CA3 just ventral to the primary start site (Fig. S4). We corrected for possible sequencing errors (see Methods, Fig. S3), resulting in 1292 unique BCs. We confirmed that sequencing depth saturated the detection of BCs in all ROIs (Fig. S3). Out of all ROIs, most FL+ cells (as quantified after imaging) and BCs were in the SSp start sites and BC overlap between areas associated with the two independent start sites (SSp and CA3) was minimal, as expected (Fig. 3C). We will here focus on ROIs associated with this primary injection site. SSp ROIs contained in total 1070 unique BCs, 757 of which were detected in SSp input sites (including 441 ghost barcodes). Assuming that each detection of a unique BC in an input site ROI, whether it was active in the start site or a ghost, described one subnetwork of a neuron in the start site, means that the experiment described up to 757 synaptic subnetworks of single SSp neurons. We detected most inputs to the SSp came from other cortical areas; including an anterior cortical region (MO/SSp, 200 BCs) and both anterior and posterior secondary somatosensory areas (SSs,

174 and 85 BCs, respectively), as well as a posterior cortical region (PTL/SSp, 178 BCs) spanning the SSp and parietal association areas (Fig. 4C-D). ROInet-seq also detected connectivity from two more distal thalamic regions, the ventral posteromedial nucleus (VPM), and dorsal thalamus (e.g., anterior- and medial dorsal nuclei).

To describe the relative architecture of each ROI's subnetworks, we next related BC detection to FL+ cells (Fig. 3C left, Fig. S4; see also Fig. 2F). We found that the ratio of FL+ cells vs. unique BCs varied greatly between ROIs. For example, the SSp start sites featured the highest number of unique BCs (340 and 390, with an overlap of 110), but FL+ cells outnumbered BCs detected in the same area ~2-fold (915 and 712, respectively). This suggests a large number of presynaptic cells in the start site, and hints that each SSp starter cell received multiple local inputs from within the SSp (Fig. 3C; convergence in Fig. 2F). Outside the start sites the ratio was typically reversed, with some variability (Fig. 3C-D). For example, from 4 FL+ cells imaged in the anterior cingulate area (ACA), we detected 23 unique BCs ($N_{BC}>N_{FL+}$). In other words, anterior cingulate area input to SSp was divergent, with each ACA neuron gave input to ~5.7 different neurons in the SSp. Similarly, we collected one ROI in the posterior SSp that was on the same plane, but outside of the SSp start site (SSp_{71-74}) (i.e., negative for any AAV FL signal). This ROI featured only 13 FL+ cells, but 85 unique BCs; meaning that each neuron in this local cluster gave input to on average ~6.5 SSp cells (divergent). One ROI in the SSp just anterior to the start site (SSp ant) had the opposite trend, where an average of 3.1 anterior SSp neurons convergently gave input to the same SSp starter cell ($N_{BC}<N_{FL+}$). In more distal thalamic input regions, we detected similar variability: Neurons of the dorsal thalamus (including AD and MD nuclei) gave divergent input, to on average ~3 SSp cells, while in the thalamic ventral posteromedial nucleus (VPM) the ratio was closer to 1. Together, combined measurement of FL+ network cells and unique BCs by ROInet-seq revealed variable, region-specific network architectures of single somatosensory cortex neurons.

So far, we used ROInet-seq to describe first order connectivity; i.e., input subnetworks from one region to the start site. However, many individual barcodes were detected in multiple input sites; i.e., identical BCs were shared between ROIs. We therefore next examined pairwise shared BCs (Fig. 3C, right, Fig. S5). In the SSp, ~35% of BCs represented higher-order network motifs (60% when disregarding ghost BCs), where the BCs were shared between two or more input sites (Fig. 3E; see multi-region inputs in Fig. 2F). In other words, ROInet-seq allowed us to detect when cells from multiple, more or less distal regions gave input to the same, single starter site neuron. We analyzed the frequency of pairs and triplets among our subnetworks and compared it to their frequency in a set of simulated networks with similar properties. Many observed pairs and triplets were significantly overrepresented, while other combinations were less likely to occur than by chance (Fig. 3F, Fig. S5). For example, out of all observed pairs, dorsal thalamus and VPM were the most overrepresented motive of synaptic convergence on single SSp neurons (Fig. 3F-H, "dors THAL + VPM"). Out of 58 BCs detected in the thalamic ventral posteromedial nucleus (VPM), 31 were also detected in other regions, and of those, 21 were shared with dorsal thalamic nuclei (e.g., AD, MD). In contrast, other SSp areas were unlikely to co-input to single SSp start site neurons together with the VPM (Fig. 3G). This observation suggests a preserved subnetwork motive, where somatosensory

cortex neurons receive simultaneous inputs from two distinct thalamic sites. Together, ROInet-seq uniquely detected and resolved higher-order input subnetworks of individual neurons from multiple remote sites; a connectivity property that cannot be obtained otherwise.

Next, we performed ROInet-seq in the hippocampus CA1 (Fig. S4, Table S2). Here, all detected inputs to the CA1 were from within the hippocampal formation, and medial septum, and most external inputs to the CA1 came from the CA3. Accurate quantification of FL+ cells was compromised by the hippocampus' dense cytoarchitecture. Nevertheless, we observed that in most input ROIs (CA1, CA3 and MS), FL+ cells outnumbered unique BCs. In other words, on average several neurons gave inputs to the same CA1 start cell (Fig. 2G, Fig. S4). Synaptic convergence to single CA1 neurons from distinct ROIs was less pronounced than in the cortex, and most BCs were detected in 1 input ROI only. Yet, we found co-inputs from several regions to the hippocampus CA1, such as from the medial septum (MS) and CA3 (Fig. S4).

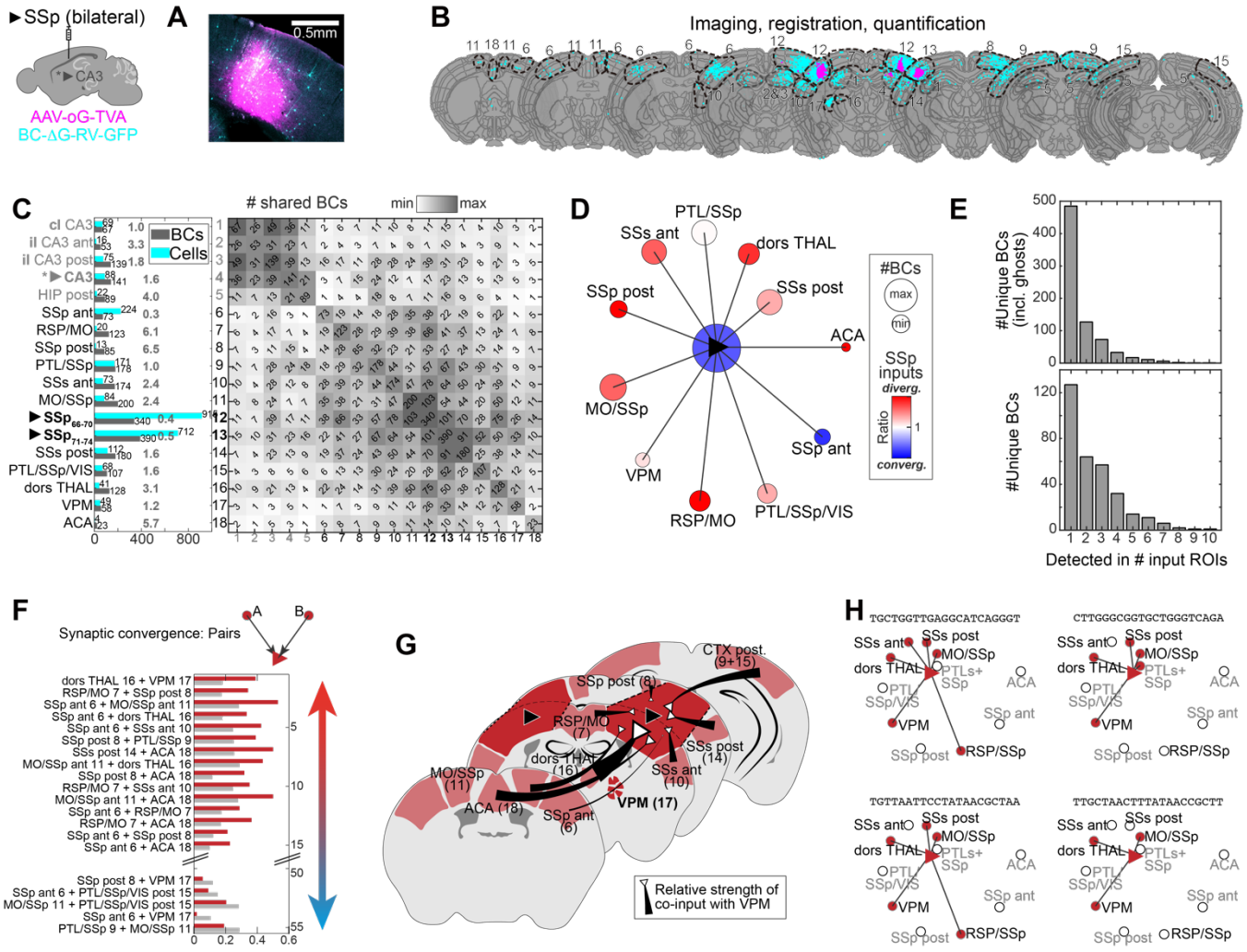

Figure 3 | Distal thalamic co-inputs to single neurons of the primary somatosensory area (SSp) discovered by ROInet-seq. (**A**) Location of primary start site in the SSp, marked by coexpression of oG, TVA helper virus (mCherry+), and BC-ΔG-RV (GFP+). (**B**) Registration of start cells (pink) and BC-ΔG-RV-infected cells (cyan), and the locations of ROIs, in eight representative a.-p. sections. (**C**) Cells and BCs detected per ROI (left), and overlap of BCs between the ROIs (right). Greyscale represents minimum to maximum values

(**Figure 3 continued**) standardized per ROI (excluding the diagonal); numbers are absolute counts of overlapping BCs per pair of ROIs. (**D**) Inputs of 11 ROIs to the SSp start site, detected in ROInet-seq as shared BCs. Circle size represents unique BCs quanitfied in the ROI, color represents the ratio of unique detected BCs to FL+ cells in the ROI; ranging from divergent- to convergent-like SSp input network motifs. (**E**) Quantification of detection of unique BCs in one, or multiple ROIs; shown for all BCs (including ghost BCs; top) or BCs also detected in start sites, only (bottom). BCs detected in multiple ROIs indicate synaptic co-inputs from multiple ROIs to single SSp start site cells. (**F**) Examples of synaptic convergence from two ROIs (indicated on the left) to single neurons in the SSp. X-axis, combination frequency, normalized to the maximum possible obeservations. Red, experimental observation of each pair; grey, random model (average of 1000 simulations). Pairs are ordered by significance, showing the top 15 (overrepresented compared to random model), and bottom 5 (underrepresented) pairs. (**G**) Spatially resolved representation of co-connectivity with VPM inputs to the SSp (synaptic convergence), on four representative coronal sections. Note that all ROIs were collected bilaterally and pooled. ROIs are highlighted in red, and arrow thickness indicates the normalized frequency of co-inputs per ROI with the VPM. (**H**) Single, unique BCs as examples of co-inputs to the SSp from the distal input site thalamic VPM, and other ROIs. Of 31 VPM barcodes with muli-input detection, 21 were also detected in dorsal thalamic regions.

To better resolve local connectivity within the hippocampus' dense cytoarchitecture we then applied the ROInet-seq principle on a commercial platform. We combined BC-ΔG-RV network tracing with the sequencing-based Visium spatial transcriptomics (ST) array (10x Genomics). We injected BC-ΔG-RV in the CA1 (unilateral), and collected 10μm fresh-frozen cryosections to the Visium capture area (Fig. 4A). A chip of four 6.5x6.5mm capture areas accommodated 16 coronal sections spanning the anterior-posterior axis of the hippocampus at 100μm spacing. We followed the Visium ST protocol to generate transcriptome-wide cDNA libraries with spatial indices. In addition, we specifically amplified the ORFs of AAV optimized glycoprotein (*oG*) and RV matrix (*M*)-gene (flanked in its 3'UTR by the BC sequence) (Fig. S6). The final sequencing library allowed us to detect transcriptome-wide gene expression, network BCs, and viral infection, spatially resolved to capture spots that typically contained several cells (diameter 55μm, center-to-center 110μm). Visium ST did not allow for imaging of native fluorescence, so viral infection was confirmed *post hoc*, using *in situ* hybridization (osmFISH) (Codeluppi et al. 2018) against RV M-gene on adjacent sections collected to separate slides (Fig. 4B).

In total 18177 capture spots (the ROIs), Visium ST detected 629 BCs, distributed over 1848 spots. Most BCs were detected in 5 spots or less, and each BC spot commonly featured 1 or 2 BCs (Fig. 4C). Along the hippocampus' anterior-posterior axis, BCs were typically restricted within <200μm, although 13 were detected across 1500μm sampled (Fig. 4D). Section 11 was most focal to the injection site but featured an unexpectedly low number of BCs (Fig. 4D). In the same section, we detected signs of visible tissue damage, and the epicenter of upregulated inflammatory genes, such as *Cxcl13* and *Lcn2* (Fig. S6). We speculate that this stress likely also led to cell death around the injection site, which would in turn inhibit detection of start site BCs, and cause ghost BCs, as observed in the SSp.

Based on previous observations in histology, we biased Visium ST sampling for better coverage anterior to the expected injection site. Reassuringly, also the spread of BCs relative to the injection site suggested that within the hippocampus, inputs to the CA1 tended to be more anterior than posterior (Fig. 4D). We

observed two main modes of input connectivity to the CA1; (i) widespread, or (ii) localized. The most abundantly detected BCs in the dataset, representing the best-connected starter neurons, typically also had the widest a.-p. spread (Fig. 4E). Most of the 16 most abundant BCs spanned inputs over at least 1000μm of the hippocampus' a.-p. aspects and were preferentially located in the CA1 (Fig. 4E-G). For example, BCs 233, 235, 315 and 447 represented CA1 neurons that

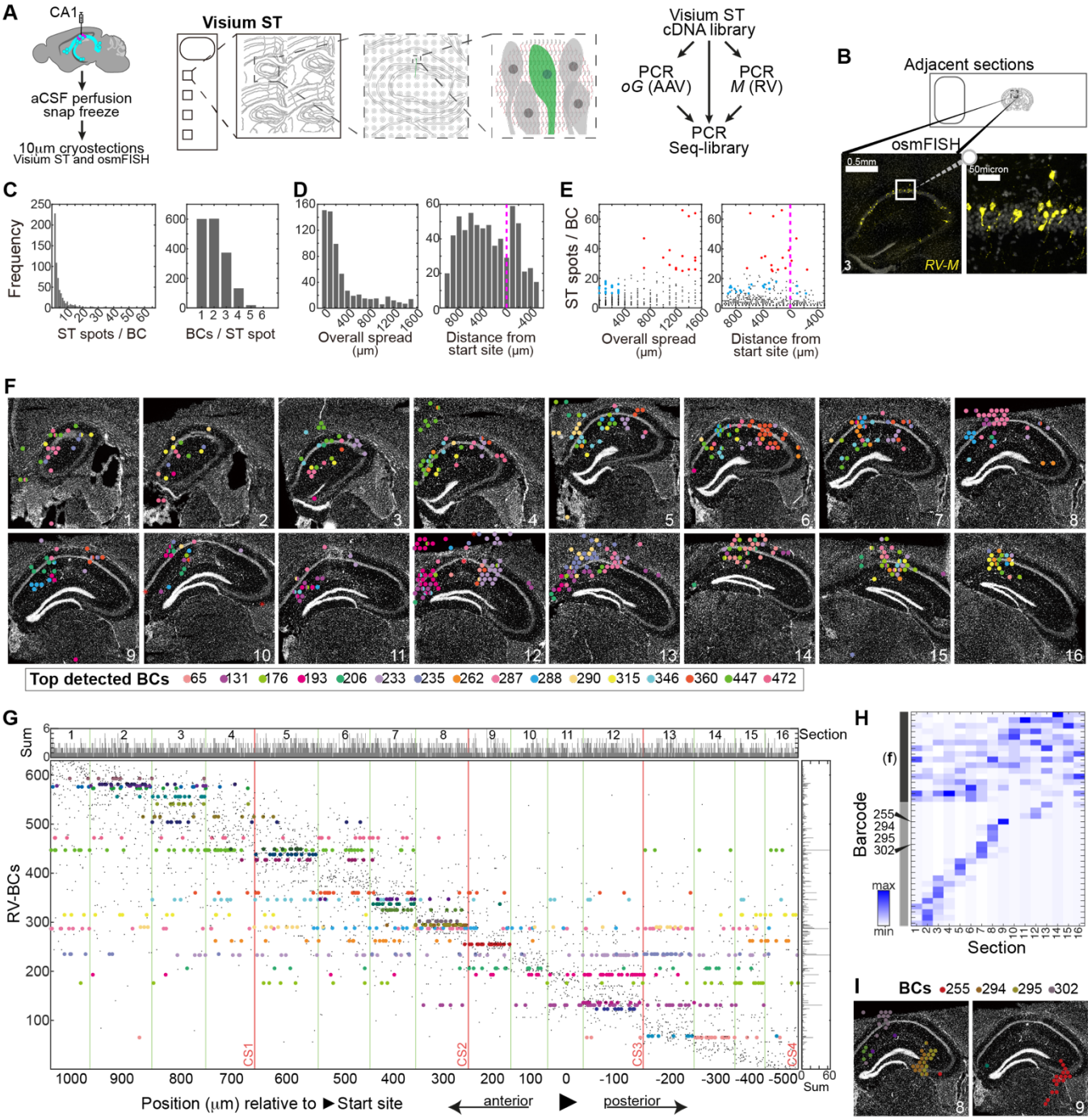

Figure 4 | Visium Spatial Transcriptomics (ST) for increased resolution of local network reconstruction. (**A**) Experimental outline Visium ST experiment: Collection of 16 coronal cryosections of the hippocampus, spanning the anterior-posterior axis, at 100μm spacing. Per ST capture area, 4 sections were collected. After cDNA library construction, sequences of interests (AAV and RV) were enriched, and sequenced. (**B**) Validation

received monosynaptic inputs from across at least 1500μm of the CA1. On the other hand, lower detected BCs, representing less-connected starter neurons, often received inputs from a single site in the CA1 or CA3 that was typically anterior to the start site (Fig. 4H-I, Fig. S6). Together, our findings suggest that even within the hippocampal formation, CA1 neurons can exhibit substantially distinct input network architectures; from a single CA3 input to remarkably widespread inter-CA1 inputs spanning large anterior-posterior distances.

(**Figure 4 continued**) of RV-infection in sections consecutive to the Visium ST-sampling, using single molecule FISH (osmFISH) against the RV matrix gene (*M*). Example and zoom-in on osmFISH section adjacent to Visium ST section 5. (**C**) Detection of RV-barcodes (BCs) in Visium ST: left, detection of barcodes in ST spots, where most BCs were restricted to 5 spots; and right, number of BCs per spot, where most RV+ spots contained one or two barcodes. (**D**) Left, distribution of total spreading distance of barcodes; and right, spreading distance relative to the start site. (**E**) Left, scatter plot of quantified barcode detection, by total spreading distance, and right, scatter plot of quantified barcode detection, by relative position to the start site (average per BC). Every spot represents one barcode; red labels the top 16 most abundantly detected BCs, blue, 22 of the most locally restricted BCs. (**F**) Spatially resolved detection of the top 16 abundant barcodes (red in (**E**)), in 16 a.-p. hippocampus sections of Visium ST; white, nuclei counterstain (DAPI). (**G**) Distribution map of all 629 detected barcodes (rows), across all RV+ 1848 Visium ST spots (columns), across the 16 a.-p. sections. (**H**) Detection of 16 top detected (top) and 22 locally mapping (bottom) BCs (rows), across 16 a.-p. sections (columns). Blue, high; white, low. (**I**) Examples for local networks of four BCs (indicated in (**H**)), mapped to 2 sections.

Discussion

We presented a high-throughput, accessible tool to map the network architecture of single-neurons across the brain, or more focused subregions at higher resolution. ROInet-seq is highly scalable: It is compatible with standard histology workflows, requires simple molecular biology processing and relatively shallow sequencing. This way, unlike a recent study using *in* situ sequencing (Zhang et al. 2023), ROInet-seq was able to reconstruct neuronal networks of single cells that spanned large distances of the brain; including networks that linked several remote sites. Leveraging combined quantification of network neurons by imaging and unique network tags (barcodes) by sequencing additionally revealed diverse network modes.

At the loss of spatial context, single-cell RNA-seq could be applied to sequence BC-ΔG-RV+ neurons across the full brain. Yet, similar to our own experience, (Zhang et al. 2023) report that insufficient cell recovery in dissociation makes reconstruction of neuronal networks too sparse. Further, the quality of RV-infected transcriptomes was compromised, likely also because of RV-infected neurons' sensitivity to the dissociation protocol. Thus, in addition to the benefit of retaining spatial context, *in situ* approaches with BC-ΔG-RV such as ROInet-seq may yield higher recovery of network cells – making them a potent *in vivo* network mapping tool.

To showcase networks that benefit from higher spatial resolution we therefore demonstrated the ROInet-seq principle on the Visium ST array. Visium ST enabled more accurate resolution of local BC-ΔG-RV labelled networks than the manual ROInet-seq approach, and reasonably allowed for representative anterior-posterior sampling of a restricted brain region. The approach spatially mapped specific BCs to histological sections, and in this way, visualized sets of small ROIs (spots) that were connected

to the same starter cell; representing subsets of a monosynaptic input network to single CA1 neurons.

Future implementations of ROInet-seq can benefit from improved versions of modified rabies virus. The N2C-RV strain both reduced cytotoxicity and increased transsynaptic efficiency (Reardon et al. 2016; Sumser et al. 2022), and a recent double-deletion modification to the B19 strain led to 90% survival of infected cells over 12 weeks and enabled long-term recordings of presynaptic and starter cells (Jin et al. 2024). Combined improvements in neuronal survival and comprehensive network labelling could make BC-ΔG-RV suited to study functional problems in neuroscience, where a sensitive, quantitative approach to connectivity is required. In addition, accessibility and application of spatial transcriptomics tools continue to be greatly hampered by cost, resolution, or throughput. Yet, given the field's rapid development (A. Chen et al. 2022; Rodriques et al. 2019; Stahl et al. 2016; Stickels et al. 2021; Vickovic et al. 2019), spatial transcriptomics is soon likely to overcome these remaining trade-offs and together with BC-ΔG-RV achieve brain-wide mapping of neuronal networks at cell, and cell-type resolution.

Limitations of the study

ROInet-seq can leverage the combined quantification of labelled network cells by imaging, and sequencing. However, both measurements are sensitive to detection, such as thresholds and segmentation in image analysis and sequencing depth and application of more or less stringent filters. Therefore, we see their ratio as a qualitative indicator, but believe it is inappropriate to derive quantitative conclusions, especially between independently conducted experiments.

We also note that any approach to cell-resolved reconstruction of synaptic networks navigates the trade-offs between spatial resolution, cell recovery and sequencing costs. ROInet-seq, while the complexity of the barcode virus library allowed detection of single-neuron networks, is not compatible with single-cell transcriptomics. Instead, the sequencing resolution of ROInet-seq represented a bulk (ROI) measurement and is unable to link network information to the cell-type identity of network neurons. Given the immense diversity of neuronal cells in the brain which are readily characterized by single-cell RNA-seq (Bakken et al. 2021; Siletti et al. 2023; Yao et al. 2021; Zeisel et al. 2015; 2018), this link will be critical to implement. Combining BC-ΔG-RV with spatial transcriptomics technologies may bridge this gap – but some drawbacks of the Visium ST approach presented here include incompatibility with native fluorescence imaging and its limited coverage at high cost. Further, since each 55μm capture spot still represents the bulk of several cells' transcriptomes, the detected network BCs could not be linked to cell type information.

Acknowledgements

This research was supported by the European Research Council (TYPEWIRE-852786 to A.Z.) and Human Frontiers Science Program (CDA-0039/2019-C to A.Z.). We thank the FACS unit of the Technion LS&E Infrastructure Center for technical assistance, and former Zeisel lab member Etay Aloni for critical discussion.

Author Contributions

L.Z., H.H. and A.Z. designed the study and planned experiments. L.Z. performed *in vitro* validation, viral injections, histology and ROI-microdissections, osmFISH and Visium ST. O.O. and P.P. performed ROInet-seq, O.O. also performed *in vitro* validation and Visium ST. T.T., B.B. and C.T. designed and performed RV library preparations and optimizations, H.S. constructed

and produced RV plasmid libraries. H.H. performed scRNA-seq. L.Z. and A.Z. analyzed *in vitro* validation data and ROInet-seq data, A.Z. and H.H. analyzed scRNA-seq data, M.T. analyzed Visium ST data. L.Z., H.H. and A.Z. interpreted all data. H.H. and L.Z. assembled figures and wrote the paper, with help from A.Z. and input from all authors.

Declaration of Interest

The authors declare no competing interests.

Methods

Mice and ethics

Adult wild-type C57BL/6JOlaHsd mice (6-8 weeks, females) were purchased from Envigo and were group housed at the Technion SPF Pre-Clinical Research Authority under standard conditions in a 12-h light:dark cycle, at ambient temperature 21-23°C and and 30-40% relative humidity. Standard chow and water were provided *ad libitum*. All animal procedures followed the legislation under the National Institute of Health guidelines and were approved by the Institutional Animal Care and Use Committee of the Technion Israel Institute of Technology.

Plasmid library generation ΔG-SAD-B19

A DNA fragment of 263bp was amplified with Pfu from vector D150pSADdeltaG-GFP-F2-ins1 using the primers:
N21Bsi2:
ccctcgctgctcgtacggtgnnnnnnnnnnnnnnnnnnnn
GTGTCAGATTATATCCCGCA
N30Pst: GGCGATGGATCCTGCAGGTCC
The amplified DNA from 8x 50µl PCR tubes was purified with 8x DFH300 silica column (Geneaid Biotech). The total yield was 3.4µg. 486ng of the purified PCR fragments where digested with BsiWI and PstI and cloned into the corresponding restriction sites of 18µg plasmid D151pSADdeltaG-GFP-F2-ins2 in a total volume of 60µl. Chemical competent E. coli cells (XL1-Blue MRF´ Kan, Agilent) were prepared by the method of Inoue *et al.* (Inoue, Nojima, and Okayama 1990). To 60 tubes with 50µl cells 1µl ligation reaction was added, incubated for 5min, heat shocked at 42°C and regenerated for 20min with 450µl SOC medium. An aliquot of the collected transformation reactions was used to calculate the complexity of the library, which was around 812.000 transformated cells. The cells from one plate were harvested with 5ml TB-medium and grown in 100ml TB-medium for 6h to an OD600 of 1. About 7.5mg DNA was isolated from 2L cells with the Megaprep Kit (Macherey Nagel).

Barcoded ΔG-SAD-B19 rabies virus generation

Pseudotyped Rabies virus particles were prepared at the Viral Core Facility of the Charité – Universitätsmedizin Berlin (vcf.charite.de) using standard protocols (Osakada and Callaway 2013). Briefly, in order to recover G-deleted rabies virus from cDNA, B7GG cells (gift from Edward Callaway, Salk Institute) were transfected with a mix of the rabies virus genomic vector D151pSADdeltaG-GFP-F2-ins2 (Barcode vector BR-16) or D151pSADdeltaG-BFP-F2-ins2 (BR-17) (internal numbering), pcDNA-SADB19N (Addgene plasmid # 32630), pcDNA-SADB19P (Addgene plasmid # 32631), pcDNA-SADB19L (Addgene plasmid # 32632) and pcDNA-SADB19G (Addgene plasmid # 32633). All vectors were gifts from Edward Callaway. Transfection was performed with Lipofectamin 3000 (ThermoFischer Scientific).

BR-16.1

Three days after transfection of three 75cm^2 flasks (80% confluency), cells were transferred into three 175cm^2 flasks. After 3 to 4 days

supernatant was collected and 15ml per flask were used for infection of another three 175cm^2 flasks (80% confluency). This was repeated 4 more times to amplify the virus. Finally, five 175cm^2 flasks (80% confluency) were used for the infection with the 7ml amplified virus supernatant. After inoculation of further 4 days the supernatant was harvested and filtered through a 0.45µm filter.

BR-16.2 / BR-16.3

Three days after transfection of three 75cm^2 flasks (80% confluency), cells were transferred into three 175cm^2 flasks. After 3 to 4 days supernatant was collected and 20ml per flask were used for infection of another two 175cm^2 flasks (80% confluency). This was repeated 2 more times with four 175cm^2 flasks to amplify the virus. After inoculation of further 4 days the supernatant was harvested and filtered through a 0.45µm filter.

BR-16.4 / BR-16.5 / BR-16.6 and ***BR-17.1***

Three days after transfection of ten 75cm^2 flasks (80% confluency), cells were transferred into ten 175cm^2 flasks. After 4 days supernatant was collected filtered through a 0.45µm filter and concentrated by ultracentrifugation (22K rpm, SW32 rotor, Beckmann). 2ml per flask were used for infection of another four 175cm^2 flasks. After inoculation of further 4 days the supernatant was harvested and filtered through a 0.45µm filter. Production of BR-17.1 was identical, except that GFP in the rabies virus genome vector used had been replaced with BFP.

For pseudotyping the rabies with the envelope protein EnvA of the Avian Sarcoma and Leukosis virus (ASLV) the obtained supernatant containing unpseudotyped viruses was applied onto ten 175cm^2 flasks containing BHK-EnvA cells (90% confluency) (gift from Edward Callaway, Salk Institute) for 5h followed by a transfer of the cells into new flasks with fresh media. After one day, media was changed a second time. After further 2 days EnvA-pseudotyped rabies viruses containing supernatant was collected, filtered and concentrated by ultracentrifugation. Rabies virus titer was determined by infecting a serial dilution of the virus in HEK293T-TVA cells (gift from Edward Callaway, Salk Institute).

Quality control barcoded ΔG-SAD-B19 *in vitro*

Barcodes counting is based on bulk amplicon sequencing. Briefly, HEK-TVA cells were infected with barcoded ΔG SAD-B19. 48hr later, ~20% of the cells were infected with rabies. Cells were then trypsinized and aliquoted into 10^5 cells per vial. Total RNA was extracted from 5 vials of cells with the RNA extraction kit (NucleoSpin, Macherey Nagel). To count the barcode number of each library, we reverse transcribed the RV-*M*-gene, using an *M*-complementary primer with the Trueseq Read 1 sequence, and a 12bp UMI (T1-UMI-RV_*M*). First-strand was carried out on 40ng total RNA, in a 20µl reaction (20U/µL Maxima H Reverse Transcriptase (Thermo), 2.5mM dNTP, 1µM T1-UMI-RV_M, 1M Betaine, 6mM MgCl2 and 2U/µL RNAse Inhibitor), incubated 45min at 50°C, 5min at 85°C, then 4°C; followed by clean-up with 2x SPRI beads, and eluted in 10µl EB. Next, the RV barcoded region was amplified with primers complementary to RV-*M* gene RV_M-T2-PCR-forward (introducing Truseq 2) and Truseq 1 (T1-PCR-reverse) in a 20µl reaction (1x KAPA, 0.5M Betaine, 0.5µM primer mix), 3min 98°C, then 16 cycles of 15sec 98°C, 20sec 60°C, 1min 72°C, finally 1min 72°C, followed by 1.2x SPRI beads cleanup, and elution in 10µl EB. Finally, sequencing adaptors P5 and P7 were introduced following the 10xGenomics dual-index setup: 20-50ng PCR product was added to library PCR mix (50% KAPA, 10% Betaine, 20% primer Dual index (Illumina)), total 20µl; 45sec 98°C, then 16 cycles of 20sec 98°C, 30sec 54°C, 20sec 72°C finally 1min 72°C. PCR was followed by double-

sided SPRI clean-up (0.6x SPRI and 0.8x SPRI). Amplicon libraries were sequenced on Illumina NextSeq2000.

Viral injections

In vivo barcoded monosynaptic tracing is based on two stereotactic injections for AAV helper virus and RV respectively as described previously. Briefly, surgeries were performed on naïve C57BL/6 mice, aged 6-8 weeks. Mice were anesthetized using isoflurane, and maintained on 1.8% isoflurane (SomnoSuite Kent Scientific). Anaesthetized mice were fixed onto the stereotactic rig (Neurostar). Optic ointment (Duratears) was applied on both eyes and body temperature was maintained at 37°C with a heating pad. We observed heart rate and oxygen saturation throughout the procedure. Craniotomy was performed after applying Lidocain/Bupivacaine to the skull for local pain relief, with a 200µm diameter drill. Virus was injected with pulled glass pipette at steady rate (25-50nl/min). After injection, we waited 8-10 min before withdrawing, to prevent reflux. Target coordinates were obtained from The Mouse Brain in Stereotaxic Coordinates, 3rd edition, Keith B.J. Franklin, George Paxinos. Buprenorphine (0.05-0.1mg/kg) was given for analgesia on the day of surgery and the day after. 21±4 days after AAV injection, RV was injected to the same target, following the same surgical procedure. Brains were harvested 7±1 days after RV injection.

For the first surgery, we used one of the following helper viruses, generated by the VVF Zürich: ssAAV-8/2-hCMV-hHBbI/E-TVA_mCherry_2A_oG-hGHp(A) (v534 serotype 8, VVF Zürich). pAAV-CMV-TVAmCherry-2A-oG was a gift from Marco Tripodi (Addgene #104330) (Ciabatti et al. 2017). ssAAV-2/2-hSyn1-hHBbI/E-TVA950_mCherry_2A_oG-hGHp(A) (v634 serotype 2, VVF Zürich; promoter altered from v534). Details for BC-ΔG-RV libraries are provided in the section "Barcoded ΔG-SAD-B19 rabies virus generation".

scRNA-seq of barcoded ΔG-SAD-B19 injected brains

To isolate single BC-ΔG-RV (GFP-library BR-16.1) infected cells for scRNA-seq, we modified a protocol for gentle adult neuron dissociation (Hochgerner et al. 2023). 8 days after bilateral stereotaxic injections to the CA1, one mouse was sacrificed by an overdose of Ketamine/Xylazine, and transcardially perfused with ice-cold carboxygenated NMDG-aCSF (Ting et al. 2014). The brain was extracted, then mounted and sectioned on a Leica VT1200S automated vibrating microtome, to 500µm slices. Fluorescent regions were quickly microdissected in ice-cold aCSF under a fluorescent stereomicroscope (Nikon SMZ18). Next, collected tissue pieces were digested in 800-100µl papain digest solution with DNase (Worthington Papain system, concentrations as recommended by manufacturer, but vials were reconstituted in aCSF), 25min at 35-37°C. Starting 15min into incubation, tissue was gently aspirated in wide-bore fire-polished Pasteur pipettes and returned to incubate, until most tissue easily broke apart. We filtered the suspension through a 30µm strainer (CellTrix, Partec) to ice-cold microtubes coated with 30% BSA, and pelleted cells at 4°C, 5min, 200g. Supernatant was fully removed, cells immediately resuspended in 500µl fixative (DSP and SPDP in sodium phosphate buffer pH8.4) (Gerlach et al. 2019), and incubated 40min, at RT, gently shaking. The fixation was stopped with 1 volume quenching buffer (0.1M Tris-HCl 150mm NaCl, pH7.4) 10min, fixed cells pelleted, and resuspended in PBS with 0.3%BSA and 1% recombinant RNase inhibitor (RRI, Takara Bio). Next, we enriched for GFP+ cells on a FACS Aria II (BD), or Bigfoot Spectral Cell Sorter (Thermo

Fisher). ~19k sorted cells were immediately processed for encapsulation and scRNA-seq on the 10xChromium NextGEM, in two samples, following the manufacturer's instructions. Libraries were sequenced on the Illumina NovaSeq NGS platform, at a depth of ~60K reads per cell.

Histology and ROInet-seq

Histology: 7d after RV injection, mice were sacrificed after an overdose of Ketamine/Xylazine, and transcardially perfused with PBS followed by 4% paraformaldehyde (PFA). Brains were dissected, postfixed in 4% PFA overnight and cryoprotected in 30% sucrose solution with PBS for 24 hr. After OCT embedding, brains were cryosectioned full-volume to 50µm floating sections, mounted to Superfrost Plus slides (Epredia), counterstained (NucBlue, Thermo) and coverslipped (Fluoromount-G, Thermo). Images were taken using an epifluorescence microscope (Nikon Eclipse Ti2) at 4x magnification. Slides were stored at -80 °C until further use.

ROI microdissection and lysis: For ROInet-seq, coverslips were gently removed in PBS, and under a fluorescent stereoscope, ROIs (tissue with RV-tagged cells) were microdissected on ice into stripes filled with lysis buffer (30mM Tris-HCL pH 7.5, 10mM EDTA, 1% SDS, 0.1µg/µl Proteinase K). Dissected tissue was vortexed vigorously and lysed for 1h at 50°C, followed by 10min at 70°C, then placed on ice. Lysates were stored at -80°C until further use.

Bead preparation and polyA capture: To capture all polyA-transcripts, introduce a 12bp UMI, 16bp ROI-specific indexes, and Truseq read 1, we loaded RT-primer (T1-ROI_index UMI-OdT) to Streptavidin beads, as follows. First, Streptavidin-C beads (5µl per ROI, Thermo) were washed twice with 2xBWT buffer (10mM Tris-HCl pH 7.5, 1mM EDTA, 2M NaCl) and resuspend with equal volume of 2xBWT buffer. In separate wells, 3µl of each unique RT primer (T1-ROI_index UMI-OdT) were added to 5µl washed beads, completed with UPW to total volume of 10µl, mixed and incubated for 20min in room temperature, 1200rpm. After incubation, RT primer-loaded beads were magnetically immobilized and washed with TNT (20mM Tris-HCl pH 7.5, 50mM NaCl, 0.02% Tween 20) and resuspend with Capture mix (50µl per ROI_index: 2xBWT, 0.5U/µl RRI (Takara)). Equal volume of lysate was added to capture mix and incubated for 1min at 56°C followed by 20min incubation at room temp, shaking 2000rpm. After incubation beads were placed on a magnet, supernatant was removed and beads were washed thoroughly 3x with ice-cold LiWT buffer (10mM Tris-HCl pH 7.5, 1mM EDTA, 150mM LiCl) and resuspend with 10µl UPW (suitable for 3 reactions). RT primers with captured polyA-transcripts were released from beads by 2min incubation at 80°C, and transferred. Samples were stored at -80°C until further use.

Reverse transcription: Reverse transcription was carried out on 2.7µl sample, by adding RT mix (1x Maxima buffer, 20U/µl Maxima enzyme, 1M Betaine, 2mM dNTPs, 2U/µl RRI, 20mM DTT, 6mM MgCl2) to a total reaction volume of 6µl, and incubating 45min at 50°C, 5min at 85°C, then 4°C.

Clean-up: After RT, samples were cleaned up using 2x volumes CleanUp buffer (5 : 1 volumes of SPRI : Guanidine Thiocyanate 6M solution) by 10min incubation followed by 2x 30sec 80% ethanol wash using bead magnet, 1min air dry and elution with 7.4µl elution solution 1 (1x Reducing Agent B (10xGenomics), 0.01% Tween-20 in buffer EB (Qiagen)).

PCR amplification: The RV barcoded region was amplified with primers complementary to RV-*M* gene (introducing Truseq read 2) and Truseq read 1, as follows. The eluate was added to 12.6µl PCR mix (1x KAPA HS, 0.5M Betaine.

Total reaction volume 20μl) with 1μM primers (RV_M-T2-forward and T1-PCR-reverse), for targeted amplification of the RV M-gene with BC; 3min 98°C, then 17 cycles of 15sec 98°C, 20sec 60°C, 1min 72°C, finally 1min 72°C. After PCR, samples were cleaned with 1.2x SPRI protocol and finally eluted in 10μl EB. Sample concentration was evaluated using Qubit.

Library indexing and sequencing: Finally, sequencing adaptors P5 and P7 were introduced following the 10xGenomics dual-index setup: 20-50ng PCR product was added to library PCR mix (50% KAPA, 10% Betaine, 20% primer Dual index (Illumina)) total 20μl; 45sec 98°C, then 16 cycles of 20sec 98°C, 30sec 54°C, 20sec 72°C finally 1min 72°C. At this point, all ROI samples were pooled to one tube, followed by double-sided SPRI clean-up (0.6x SPRI and 0.8x SPRI). Concentration was evaluated using Qubit and fragment size on Bioanalyzer or TapeStation. The final ROIs amplicon libraries resemble 10xChromium v3/NextGEM sequencing libraries and were sequenced at a depth of ~10M reads per sample (one brain) on Illumina NextSeq2000. In its final implementation, a typical ROInet-seq experiment was microdissected and processed for RNA-sequencing within 2 days (day 1, microdissection and lysis; day 2, molecular biology processing). PCR amplification introducing the final library indexes can in principle be carried out with all ROI samples in pool, as demonstrated for the experiment presented in Fig. S4. This saved ~2h of manual handling time but increased representation of noisy BCs; requiring more stringent computational processing, detailed in "ROInet-seq data processing and analysis".

ROInet-seq data processing and analysis

ROInet-seq fastq files contained ROI-index, UMI (both Read 1) and the target sequence on the 3'UTR of the RV-*M*-gene, including the BC-read (Read 2). First, we aligned ROI-index reads with the known list of ROIs wells that were collected. In Read 2, we called the BC read by aligning the known, permanent sequences flanking the BC in the *M*-3'UTR, and extracting every variable 21nt sequence inside (SSp, 1.67M BC reads; and CA1, 3.4M BC reads). This was combined to an initial, unprocessed matrix of BCs, and their counts per ROI. Next, we corrected for sequencing errors, by pooling any BCs with Hamming distance of ≤3 with its most abundant version. We filtered BCs with low confidence, by removing BCs of below 100 reads. Any BC detected above that threshold was included towards the final BC count matrix (Table S1), used to plot overlaps of BCs between ROIs, and global or single-barcode networks.

In the hippocampus CA1 experiment (Fig. S4), clean-up and the final PCR reaction were carried out in pool over all ROIs. This increased representation of noisy BCs; requiring more stringent computational processing, as follows: We first normalized ROIs to each other; accounting for the total number of reads per ROI, and the number of BCs detected in that ROI: For each ROI, the total read count was divided by the square root of the number of unique BCs in that ROI. We filtered BCs with low confidence, by removing BCs of below 200 reads. In addition, we applied a stringent exclusion of BCs from ROIs where that BC was detected below its average (plus standard deviation, ($x_{ij} - (\mu + \sigma)$, where x is the read count of BC i in ROI j)).

Spatial transcriptomics networks sequencing (Visium ST)

Transcardial perfusion with aCSF was performed under deep anesthesia on the harvest day. Brains were snap frozen on dry ice and stored at -80°C until sectioning the following day. The brain was cryo-sectioned into 20μm, by cutting only the hippocampus region and collecting to capture areas on the Visium Spatial Transcriptome slide (Fig. S6). The gap between

two consecutive sections collected to the capture area was 100µm. All adjacent sections were collected to a SuperFrost Plus Slide (Epredia) and stored at -80°C until processing. Visium ST slides were processed as per the manufacturer's instructions, with the following specifications: Slides were fixed with methanol, then DAPI counterstained and imaged on an inverted epifluorescence microscope (Nikon Eclipse Ti2). Tissue was permeabilized for 30 min. The mRNAs from the sections were then captured by the primers including UMI, spatial barcode and sequencing primer on the Visium ST slides. After the RT reaction and second strand synthesis on slides, the cDNA library was transferred into tubes, fragmented and indexed. For detection of RV-barcodes and AAV transcripts, cDNA was additionally amplified in two separate PCR reactions, with RV_M-T2-PCR-forward / T1-PCR-reverse (RV-*M*-gene) or AAV-T2-PCR forward / T1-PCR-reverse (AAV-*oG*-gene), using 20-30ng cDNA, each in a 10µl reaction (1x KAPA, 0.5M Betaine, 1µM primer mix), 3min 98°C, then 8 cycles (RV-*M*) or 10 (AAV-*oG*) cycles of 15sec 98°C, 20sec 53°C, 1min 72°C, finally 1min 72°C, followed by 1x SPRI beads cleanup, and elution in 4µl EB. Finally, sequencing adaptors P5 and P7 were introduced following the 10xGenomics dual-index setup: Eluted PCR product was added to library PCR mix (50% KAPA, 10% Betaine, 20% primer Dual index (Illumina)), total 20µl; 45sec 98°C, then 12 cycles of 20sec 98°C, 30sec 54°C, 20sec 72°C finally 1min 72°C. PCR was followed by double-sided SPRI clean-up (0.6x SPRI and 0.8x SPRI). Amplicon libraries were sequenced to 140-260M reads per sample on Illumina NextSeq2000.

Visium ST data processing and analysis

The methodology for analyzing Visium data and detecting barcodes is implemented through a comprehensive MATLAB script designed for the integration of rabies barcode information with spatial context derived from Visium experiments. It proceeds to process barcode data from distinct experimental conditions, including Vis11_A1, Vis11_B1, Vis11_C1, and Vis11_D1, as well as RFP-AAV SAM files. This involved organizing data into: cell IDs, unique sequences, and read frequencies, leading to the creation of a unified table combining rabies and AAV data. Further, since sequencing depth of individual capture spots was unequal, we next normalized spots to each other; accounting for the total number of reads per spot, and the number of BCs detected in that spot, as follows: For each spot, the total read count was divided by the square root of the number of unique BCs in that spot. Finally, we filtered noisy BCs, by removing BCs that were below an average expression threshold or had null empty entries. Genes and BCs shown in the Figures were plotted in a binary fashion, i.e., each spot with a detected gene or BC is shown positive. We further incorporate functionality to subset and process specific barcode sequences from FASTQ files, saving the resulting subset and identifying common elements with loaded barcodes. Additionally, we used DAPI images of the Visium ST sections to map each section in its anatomical context by semi-manual aligning sections to the Allen Reference Atlas—Mouse Brain (atlas.brain-map.org) and correcting for distortion caused by sectioning along the dorsoventral and mediolateral axes. Sections were on average 100µm apart. mRNA-capture spot diameters were 55µm, centers 100µm apart (x–y resolution). 18,177 capture spots covered the tissue and contained on average ~3,300 genes and ~9,900 UMIs. 1848 of the capture spots were positive for RV (expressing positive values higher than one). We called the BC read by aligning the known, permanent sequences flanking the BC in the *M*-3'UTR and extracting every variable 21nt sequence inside. We finally corrected for sequencing errors by pooling any BCs with Hamming distance of ≤3 with its most abundant version.

osmFISH

To detect viral transcripts in sections adjacent to the ones sampled for Visium ST, we performed in situ hybridization according to osmFISH (Codeluppi et al. 2018), with minor modifications. We collected 10μm sections to Superfrost Plus slides (Epredia) and stored them at -80°C until processing. After the sections were balanced at RT, the tissue was fixed in 4% PFA for 10 min, washed 5 min with 2x SSC buffer, and cleared with 8% SDS for 30 min. Tissue is incubated with hybridization mix (2x SSC, 10% dextran sulfate, 10% formamide, 1mg/ml E. coli tRNA, 2mM ribonucleoside vanadyl complexes, 0.2ml/ml bovine serum albumin) without probes for 5 min at RT and then 4h at 38.5 °C in hybridization mix with probes (250nM). After wash with 20% formamide in 2x SSC, slides were mounted (ProLong Diamond Antifade, Thermo) and imaged at 10x magnification, on an inverted epifluorescence microscope (Nikon Eclipse Ti2).

Oligonucleotide DNA sequences

Name	Sequence
T1-UMI-RV_M	TTTCCCTACACGACGCTCTTCCGATCTNNNNNNNNNNNNNTGTTATATTGCTCCCAAGGGTTGG
T1-ROI_index UMI-OdT	CTACACGACGCTCTTCCGATCTNNNNNTAGCTANNNNNNNNNNNNNNNNNNTTTTTTTTTTTTTTTTTTTTTTTTTTTTTTVN
RV_M-T2-PCR-forward	GTGACTGGAGTTCAGACGTGTGCTCTTCCGATCTGGACAAAGATTCCTCTCTGCT
T1-PCR-reverse	ACACTCTTTCCCTACACGACGCTC
AAV-T2-PCR forward	GTGACTGGAGTTCAGACGTGTGCTCTTCCGATCTGACGTGCACGAACGGATCAGTG

Data availability

The raw sequencing data generated in the current study will be made available through NCBI GEO. Source Data (BC count tables for ROInet-seq experiments) are provided as supplementary files with this paper. For convenience, we additionally provide single-cell expression dataset with annotations and metadata as a table at figshare, made available upon publication or per request.

Code availability

Custom code used to perform the analysis will be made available upon publication or per request.

Supplemental information titles and legends

Table S1 Barcode count matrix SSp. Related to Fig. 3. Barcode counts per ROI, for the ROInet-seq experiment with primary injection site in the somatosensory cortex SSp.

Table S2 Barcode count matrix CA1. Related to Fig. S4. Barcode counts per ROI, for the ROInet-seq experiment with primary injection site in the hippocampus CA1.

Fig. S1 Characterization of BC-ΔG-RV libraries.
(**A**) Sequencing verification of a uniformly random 21nt BC insert, shown as pseudo-Sanger bp frequency plot. (**B**) Accumulative frequency of the top 10k most frequent barcodes per RV-library, vs. the optimally uniform plasmid library.

(**C**) Expected detection of a unique BC in 1-12+ cells, given 8 scenarios based on 10-1000 starter cells, per library.
(**D**) Quantification of presynaptic-per-starter cells after infection to the CA1 (unilateral) with ΔG-RV (n=4; grey; 144.1 +/-88.5) and BC-ΔG-RV (n=4; black; 42.2+/-27.9).
(**E**) As (**D**), quantification of presynaptic-per-starter neurons resolved to the sections along the anterior-posterior axis. Pink line, injection coordinates.
(**F**) As (**D**), quantification of presynaptic-per-starter neurons, summed by brain region.

Fig. S2 Single-cell RNA-seq on BC-ΔG-RV-infected neurons *in vivo*.
(**A**) Experimental schematic, BC-ΔG-RV infection of hippocampus CA1, with secondary infection in isocortex dorsal to CA1, followed by dissociation, fixation, FACS and scRNA-seq; to simultaneously detect transcriptomes and BCs.
(**B**) tSNE visualization of 8032 cells, colored by cell type. Among 6979 neuronal transcriptomes, 129 were GABAergic interneurons, 2744 had a predominantly cortical pyramidal signature (1566 of which L4/5/6) and 2937 a hippocampal pyramidal signature (1418 of which CA1).
(**C**) Expression of 4 neuronal genes, *Gfp* (RV) or any one AAV-gene (*TVA, oG, mCherry*) in all cells visualized in (**B**). Grey, low; red, high; black circle, 0. Note, cluster 14 featured the highest expression of *Gfp* (RV), but overall low-quality transcriptomes with general neuronal markers.
(**D**) Frequency of detecting single or multiple BCs in a single cell; in starter cells (91 neurons, as in Fig. 1F) or all BC-ΔG-RV+ cells (total, 6310 BC+ neurons).
(**E**) Four examples of potential single-cell networks; i.e., cells sharing a unique barcode. Over all networks, most have no verified starter cell (cell with AAV and GFP detected), and most have some degree of mixing of transcriptomic types from CTX and HIP, as shown in one example.

Fig. S3 ROInet-seq processing and QC.
(**A**) Schematic of RT and BC-specific amplification from fixed tissue ROIs in ROInet-seq. Each ROI is collected to a separate well, loaded with lysis buffer and polyT primer carrying a unique ROI barcode (spatial index). In reverse transcription (RT), the indexed polyT captures polyA transcripts present in that ROI, including RV-genes such as *M* (with BC in its 3'UTR). cDNA is amplified in two consecutive PCR reactions, first using an oligo specific to a sequence flanking the *M*-gene (and BC), and then sequencing library prep to introduce library indexes and P5/P7.
(**B**) For SSp ROInet-seq presented in Fig. 3, read counts detected per ROI, including 11 blank negative control wells (top), and one ROI (globus pallidus, GP) that did not pass the threshold.
(**C**) Sorted read coverage per BC, per ROI, for all 18 ROIs (lines), in order of abundance of the BCs detected in that ROI. Outside the injection site, all ROIs reach saturation.

Fig. S4 Single-cell input networks in the hippocampus CA1 with ROInet-seq.
(**A**) Location of primary start site in the CA1, marked by coexpression of oG, TVA helper virus (mCherry+), and BC-ΔG-RV (GFP+).
(**B**) Registration of start cells (pink) and BC-ΔG-RV-infected cells (cyan), in eight a.-p. sections.
(**C**) Cells and BCs detected per ROI (left), and overlap of BCs between the ROIs (right). Greyscale represents minimum to maximum values standardized per ROI (excluding the diagonal); numbers are absolute counts of overlapping BCs per pair of ROIs. Subscripted numbers in ROI names depict a.-p. position. Black, hippocampus-associated; grey, cortex-associated (off-target start site).
(**D**) Inputs of 7 ROIs to the CA1 start site, detected in ROInet-seq as shared BCs. Circle size represents unique BCs quanitfied in the ROI, color represents the ratio of unique detected BCs to FL+ cells in the ROI; ranging from divergent- to convergent-like SSp input network motifs. Ratios widely differed across the three planes spanning the start site; so no color is shown to represent the ratio in the CA1 start site.
(**E**) Quantification of detection of unique BCs in one, or multiple ROIs; shown for all BCs (including ghost BCs; left) or only BCs also detected in start sites (right). BCs detected in multiple ROIs indicate synaptic co-inputs from multiple ROIs to single CA1 start site cells.
(**F**) Single, unique BCs as examples of co-inputs to the CA1 from the pallium's medial septum (MS) and CA3. Of 11 MS barcodes with muli-input detection, 8 were also detected in CA3.
(**G**) In the CA1 injection, off-target detection of start cells in the cortex dorsal to CA1.

(**H**) In the SSp injection (Fig. 3), off-target detection of start cells in the anterior CA3 ventral to the injection site.

Fig. S5 Pairwise overlaps of BC in ROInet-seq.
(**A**) Scatterplots of barcodes detected in 16 pairs of ROIs, as indicated on each axis. Axes units are BC reads normalized to the total reads per ROI (Reads * unique BCs detected / total BC reads). Each dot represents one BC, green depicts BCs detected in both regions. BC count sums are indicated.
(**B**) Examples of synaptic convergence from three ROIs (indicated on the left) to single neurons in the SSp. X-axis, combination frequency, normalized to the maximum possible obeservations. Red, experimental observation of each triplet; grey, random model (average of 1000 simulations). Triplets are ordered by significance (overrepresented compared to random model).

Fig. S6 Visium Spatial Transcriptomics (ST) for local network reconstruction.
(**A**) Details of experimental outline Visium ST experiment (see Fig. 4): Collection 4 coronal cryosections per ST capture area, and total 16 sections to one Visium ST slide. polyA transcripts are captured to spatially indexed polyT oligos immobilized on the capture area surface. After cDNA library construction, sequences of interests (AAV and RV) were enriched, and sequenced.
(**B**) Workflow for amplification of RV (BC) and AAV (TVA) -related transcripts, from full cDNA.
(**C**) Spatially resolved detection of 22 abundant, but locally restricted barcodes (blue in Fig. 4E), in 16 a.-p. hippocampus sections of Visium ST; white, nuclei counterstain (DAPI).
(**D**) Visium ST gene expression of RV (*Gfp*), pyramidal neuron (*Neurod6, Spink8, Lpl*) and inflammatory markers (*Lcn2, Cxcl13*) in sections 5 and 10; with single molecule FISH-validation of RV matrix gene (*M*) expression in consecutive sections shown on the left. Scale bars, 0.5mm.

References

Bakken, Trygve E., Nikolas L. Jorstad, Qiwen Hu, Blue B. Lake, Wei Tian, Brian E. Kalmbach, Megan Crow, et al. 2021. "Comparative Cellular Analysis of Motor Cortex in Human, Marmoset and Mouse." *Nature 2021 598:7879* 598 (7879): 111–19. https://doi.org/10.1038/s41586-021-03465-8.

Chen, Ao, Sha Liao, Mengnan Cheng, Kailong Ma, Liang Wu, Yiwei Lai, Xiaojie Qiu, et al. 2022. "Spatiotemporal Transcriptomic Atlas of Mouse Organogenesis Using DNA Nanoball-Patterned Arrays." *Cell* 185 (10): 1777-1792.e21. https://doi.org/10.1016/j.cell.2022.04.003.

Chen, Xiaoyin, Yu-Chi Sun, Huiqing Zhan, Justus M. Kebschull, Stephan Fischer, Katherine Matho, Z. Josh Huang, Jesse Gillis, and Anthony M. Zador. 2019. "High-Throughput Mapping of Long-Range Neuronal Projection Using In Situ Sequencing." *Cell* 179 (3): 772-786.e19. https://doi.org/10.1016/j.cell.2019.09.023.

Ciabatti, Ernesto, Ana González-Rueda, Letizia Mariotti, Fabio Morgese, and Marco Tripodi. 2017. "Life-Long Genetic and Functional Access to Neural Circuits Using Self-Inactivating Rabies Virus." *Cell* 170 (2): 382-392.e14. https://doi.org/10.1016/j.cell.2017.06.014.

Clark, Iain C., Cristina Gutiérrez-Vázquez, Michael A. Wheeler, Zhaorong Li, Veit Rothhammer, Mathias Linnerbauer, Liliana M. Sanmarco, et al. 2021. "Barcoded Viral Tracing of Single-Cell Interactions in Central Nervous System Inflammation." *Science* 372 (6540). https://doi.org/10.1126/science.abf1230.

Codeluppi, Simone, Lars E. Borm, Amit Zeisel, Gioele La Manno, Josina A. van Lunteren, Camilla I. Svensson, and Sten Linnarsson. 2018. "Spatial Organization of the Somatosensory Cortex Revealed by osmFISH." *Nature Methods* 15 (11): 932–35. https://doi.org/10.1038/s41592-018-0175-z.

Fuzik, János, Amit Zeisel, Zoltán Máté, Daniela Calvigioni, Yuchio Yanagawa, Gábor Szabó, Sten Linnarsson, and Tibor Harkany. 2016. "Integration of Electrophysiological Recordings with Single-Cell RNA-Seq Data Identifies Neuronal Subtypes." *Nature Biotechnology* 34 (2): 175–83. https://doi.org/10.1038/nbt.3443.

Gerlach, Jan. P., Jessie A. G. van Buggenum, Sabine E. J. Tanis, Mark Hogeweg, Branco M. H. Heuts, Mauro J. Muraro, Lisa Elze, et al. 2019. "Combined Quantification of Intracellular (Phospho-)Proteins and Transcriptomics from Fixed Single Cells." *Scientific Reports* 9 (1): 1469. https://doi.org/10.1038/s41598-018-37977-7.

Hochgerner, Hannah, Shelly Singh, Muhammad Tibi, Zhige Lin, Niv Skarbianskis, Inbal Admati, Osnat Ophir, et al. 2023. "Neuronal Types in the Mouse Amygdala and Their Transcriptional Response to Fear Conditioning." *Nature Neuroscience*. https://doi.org/10.1038/s41593-023-01469-3.

Inoue, Hiroaki, Hiroshi Nojima, and Hiroto Okayama. 1990. "High Efficiency Transformation of Escherichia Coli with Plasmids." *Gene* 96 (1): 23–28. https://doi.org/10.1016/0378-1119(90)90336-P.

Jin, Lei, Heather A. Sullivan, Mulangma Zhu, Thomas K. Lavin, Makoto Matsuyama, Xin Fu, Nicholas E. Lea, et al. 2024. "Long-Term Labeling and Imaging of Synaptically Connected Neuronal Networks in Vivo Using Double-Deletion-Mutant Rabies Viruses." *Nature Neuroscience*, January. https://doi.org/10.1038/s41593-023-01545-8.

Kebschull, Justus M, Pedro Garcia Da Silva, Ashlan P Reid, Ian D Peikon, Dinu F Albeanu, and Anthony M Zador Correspondence. 2016. "High-Throughput Mapping of Single-Neuron Projections by Sequencing of Barcoded RNA." *Neuron* 91: 975–87. https://doi.org/10.1016/j.neuron.2016.07.036.

Mahalingam, Gayathri, Russel Torres, Daniel Kapner, Eric T Trautman, Tim Fliss, Shamishtaa Seshamani, Eric Perlman, et al. 2022. "A Scalable and Modular Automated Pipeline for Stitching of Large Electron Microscopy Datasets." *eLife* 11 (July). https://doi.org/10.7554/eLife.76534.

Michalska, Julia M., Julia Lyudchik, Philipp Velicky, Hana Štefaničková, Jake F. Watson, Alban Cenameri, Christoph Sommer, et al. 2023. "Imaging Brain Tissue Architecture across Millimeter to Nanometer Scales." *Nature Biotechnology*, August. https://doi.org/10.1038/s41587-023-01911-8.

Oh, Seung Wook, Julie A. Harris, Lydia Ng, Brent Winslow, Nicholas Cain, Stefan Mihalas, Quanxin Wang, et al. 2014. "A Mesoscale Connectome of the Mouse Brain." *Nature* 508 (7495): 207–14. https://doi.org/10.1038/nature13186.

Osakada, Fumitaka, and Edward M Callaway. 2013. "Design and Generation of Recombinant Rabies Virus Vectors." *Nature Protocols* 8 (8): 1583–1601. https://doi.org/10.1038/nprot.2013.094.

Qiu, Shou, Yachuang Hu, Yiming Huang, Taosha Gao, Xiaofei Wang, Danying Wang, Biyu Ren, et al. 2024. "Whole-Brain Spatial Organization of Hippocampal Single-Neuron Projectomes." *Science* 383 (6682). https://doi.org/10.1126/science.adj9198.

Reardon, Thomas R., Andrew J. Murray, Gergely F. Turi, Christoph Wirblich, Katherine R. Croce, Matthias J. Schnell, Thomas M. Jessell, and Attila Losonczy. 2016. "Rabies Virus CVS-N2c ΔG Strain Enhances Retrograde Synaptic Transfer and Neuronal Viability." *Neuron* 89 (4): 711–24. https://doi.org/10.1016/j.neuron.2016.01.004.

Rodriques, Samuel G., Robert R. Stickels, Aleksandrina Goeva, Carly A. Martin, Evan Murray, Charles R. Vanderburg, Joshua Welch, Linlin M. Chen, Fei Chen, and Evan Z. Macosko. 2019. "Slide-

Seq: A Scalable Technology for Measuring Genome-Wide Expression at High Spatial Resolution." *Science* 363 (6434): 1463–67. https://doi.org/10.1126/science.aaw1219.

Saunders, Arpiar, Kee Wui Huang, Cassandra Vondrak, Christina Hughes, Karina Smolyar, Harsha Sen, Adrienne C. Philson, et al. 2022. "Ascertaining Cells' Synaptic Connections and RNA Expression Simultaneously with Barcoded Rabies Virus Libraries." *Nature Communications* 13 (1): 6993. https://doi.org/10.1038/s41467-022-34334-1.

Siletti, Kimberly, Rebecca Hodge, Alejandro Mossi Albiach, Ka Wai Lee, Song-Lin Ding, Lijuan Hu, Peter Lönnerberg, et al. 2023. "Transcriptomic Diversity of Cell Types across the Adult Human Brain." *Science* 382 (6667). https://doi.org/10.1126/science.add7046.

Stahl, P. L., F. Salmen, S. Vickovic, A. Lundmark, J. F. Navarro, J. Magnusson, S. Giacomello, et al. 2016. "Visualization and Analysis of Gene Expression in Tissue Sections by Spatial Transcriptomics." *Science* 353 (6294): 78–82. https://doi.org/10.1126/science.aaf2403.

Stickels, Robert R., Evan Murray, Pawan Kumar, Jilong Li, Jamie L. Marshall, Daniela J. Di Bella, Paola Arlotta, Evan Z. Macosko, and Fei Chen. 2021. "Highly Sensitive Spatial Transcriptomics at Near-Cellular Resolution with Slide-seqV2." *Nature Biotechnology* 39 (3): 313–19. https://doi.org/10.1038/s41587-020-0739-1.

Sumser, Anton, Maximilian Joesch, Peter Jonas, and Yoav Ben-Simon. 2022. "Fast, High-Throughput Production of Improved Rabies Viral Vectors for Specific, Efficient and Versatile Transsynaptic Retrograde Labeling." Edited by Rebecca Seal, Laura L Colgin, and Ian Wickersham. *eLife* 11: e79848. https://doi.org/10.7554/eLife.79848.

Suzuki, Toshiaki, Nao Morimoto, Akinori Akaike, and Fumitaka Osakada. 2020. "Multiplex Neural Circuit Tracing With G-Deleted Rabies Viral Vectors." *Frontiers in Neural Circuits* 13 (January). https://doi.org/10.3389/fncir.2019.00077.

Ting, Jonathan T., Tanya L. Daigle, Qian Chen, and Guoping Feng. 2014. "Acute Brain Slice Methods for Adult and Aging Animals: Application of Targeted Patch Clamp Analysis and Optogenetics." *Methods in Molecular Biology* 1183: 221–42. https://doi.org/10.1007/978-1-4939-1096-0_14.

Turner, Nicholas L., Thomas Macrina, J. Alexander Bae, Runzhe Yang, Alyssa M. Wilson, Casey Schneider-Mizell, Kisuk Lee, et al. 2022. "Reconstruction of Neocortex: Organelles, Compartments, Cells, Circuits, and Activity." *Cell* 185 (6): 1082-1100.e24. https://doi.org/10.1016/j.cell.2022.01.023.

Vickovic, Sanja, Gökcen Eraslan, Fredrik Salmén, Johanna Klughammer, Linnea Stenbeck, Denis Schapiro, Tarmo Äijö, et al. 2019. "High-Definition Spatial Transcriptomics for in Situ Tissue Profiling." *Nature Methods* 16 (10): 987–90. https://doi.org/10.1038/s41592-019-0548-y.

Wickersham, Ian R., David C. Lyon, Richard J.O. Barnard, Takuma Mori, Stefan Finke, Karl-Klaus Conzelmann, John A.T. Young, and Edward M. Callaway. 2007. "Monosynaptic Restriction of Transsynaptic Tracing from Single, Genetically Targeted Neurons." *Neuron* 53 (5): 639–47. https://doi.org/10.1016/j.neuron.2007.01.033.

Yao, Zizhen, Cindy T.J. van Velthoven, Thuc Nghi Nguyen, Jeff Goldy, Adriana E. Sedeno-Cortes, Fahimeh Baftizadeh, Darren Bertagnolli, et al. 2021. "A Taxonomy of Transcriptomic Cell Types across the Isocortex and Hippocampal Formation." *Cell* 184 (12): 3222-3241.e26. https://doi.org/10.1016/j.cell.2021.04.021.

Yin, Wenjing, Derrick Brittain, Jay Borseth, Marie E. Scott, Derric Williams, Jedediah Perkins, Christopher S. Own, et al. 2020. "A Petascale Automated Imaging Pipeline for Mapping

Neuronal Circuits with High-Throughput Transmission Electron Microscopy.” *Nature Communications* 11 (1): 4949. https://doi.org/10.1038/s41467-020-18659-3.

Zeisel, Amit, Hannah Hochgerner, Peter Lönnerberg, Anna Johnsson, Fatima Memic, Job van der Zwan, Martin Häring, et al. 2018. “Molecular Architecture of the Mouse Nervous System.” *Cell* 174 (4): 999-1014.e22. https://doi.org/10.1016/J.CELL.2018.06.021.

Zeisel, Amit, Ana B. Muñoz-Manchado, Simone Codeluppi, Peter Lönnerberg, Gioele La Manno, Anna Juréus, Sueli Marques, et al. 2015. “Cell Types in the Mouse Cortex and Hippocampus Revealed by Single-Cell RNA-Seq.” *Science* 347 (6226).

Zhang, Aixin, Lei Jin, Shenqin Yao, Makoto Matsuyama, Cindy van Velthoven, Heather Sullivan, Na Sun, et al. 2023. “Rabies Virus-Based Barcoded Neuroanatomy Resolved by Single-Cell RNA and in Situ Sequencing.” *eLife* 12. https://doi.org/10.7554/eLife.87866.1.